Optimal structuring of nitrogen-doped hybrid-dimensional nanocarbons for high-performance flexible solid-state supercapacitors — Source link ↗

Xianyi Cao, Shuai Jia, Wei Huang, Yingying Tang ...+3 more authors

Institutions: Technical University of Denmark, Rice University

Published on: 26 Mar 2019 - Journal of Materials Chemistry (The Royal Society of Chemistry)

Topics: Carbon nanotube

Related papers:

- Three-Dimensional MoS2@CNT/RGO Network Composites for High-Performance Flexible Supercapacitors

- Flexible and freestanding MoS2/rGO/CNT hybrid fibers for high-capacity all-solid supercapacitors

- Flexible solid-state supercapacitor based on reduced graphene oxide-enhanced electrode materials

- Engineering rGO-CNT wrapped Co3S4 nanocomposites for high-performance asymmetric supercapacitors

- Flexible free-standing 3D porous N-doped graphene-carbon nanotube hybrid paper for high- performance supercapacitors†

DTU Library

Optimal structuring nitrogen-doped hybrid-dimensional nanocarbons for high-performance flexible solid-state supercapacitors

Cao, Xianyi; Jia, Shuai; Tang, Yingying; Duus, Jens Øllgaard; Lou, Jun ; Chi, Qijin

Journal of Materials Chemistry A

Accepted Manuscript

Volume 4 | Number 1 | 7 January 2016 | Pages 1–330

Journal of
Materials Chemistry A

Materials for energy and sustainability
www.rsc.org/MaterialsA

ISSN 2050-7488

ROYAL SOCIETY OF CHEMISTRY

PAPER
Kun Chang, Zhaorong Chang et al.
Bubble-template-assisted synthesis of hollow fullerene-like
MoS₂ nanocages as a lithium ion battery anode material

175 YEARS
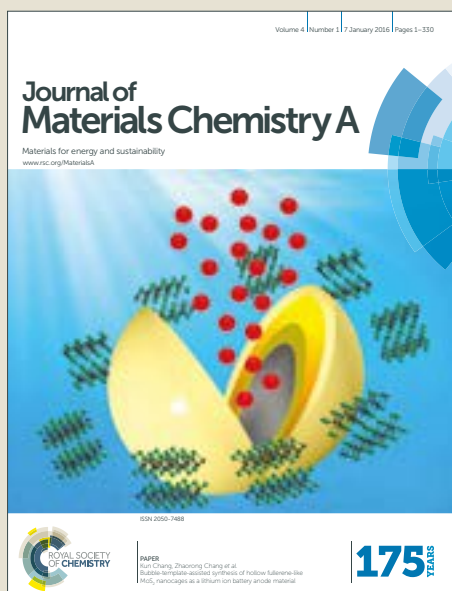
This is an Accepted Manuscript, which has been through the Royal Society of Chemistry peer review process and has been accepted for publication.

Accepted Manuscripts are published online shortly after acceptance, before technical editing, formatting and proof reading. Using this free service, authors can make their results available to the community, in citable form, before we publish the edited article. We will replace this Accepted Manuscript with the edited and formatted Advance Article as soon as it is available.

You can find more information about Accepted Manuscripts in the **author guidelines**.

Please note that technical editing may introduce minor changes to the text and/or graphics, which may alter content. The journal's standard **Terms & Conditions** and the ethical guidelines, outlined in our **author and reviewer resource centre**, still apply. In no event shall the Royal Society of Chemistry be held responsible for any errors or omissions in this Accepted Manuscript or any consequences arising from the use of any information it contains.

ROYAL SOCIETY OF CHEMISTRY

rsc.li/materials-a

Journal of Materials Chemistry A

PAPER

Optimal structuring nitrogen-doped hybrid-dimensional nanocarbons for high-performance flexible solid-state supercapacitors†

Xianyi Cao,[a] Shuai Jia,[b] Wei Huang,[a] Yingying Tang,[a] Jens Øllgaard Duus,[a] Jun Lou,*[b] and Qijin Chi*[a]

The rapid development of wearable electronics has increasingly demanded high-performance flexible power-supply devices for enhancing portability and durability. Flexible solid-state supercapacitors (FSSSCs) could have potential to fulfill this demand, but engineering electrode materials is still a challenging issue. Herein, we demonstrate optimal structuring nitrogen-doped hybrid-dimensional nanocarbons (N-RGO-CNT-CBNP) for high-performance FSSSCs. Three types of representative nanocarbons including reduced graphene oxide nanosheets, carbon nanotubes and carbon black nanoparticles are explored as building blocks to construct N-RGO-CNT-CBNP synergistically via facile and low-cost solution processing. With melamine as both a structure-directing agent and a highly effective nitrogen source, a highly-porous three-dimensional hierarchical structure and a high nitrogen doping level of 13.8 at.% are simultaneously achieved. Such a nanostructured material is employed to fabricate sandwich-structured papers (N-RGO-CNT-CBNP-Ps) with high flexibility, conductivity and mechanical strength. The resulting N-RGO-CNT-CBNP-Ps possess an ultrahigh areal specific capacitance (935 mF cm^{-2} at 1 mA cm^{-2}), as well as remarkable rate capability (e.g. 580 mF cm^{-2} at 100 mA cm^{-2}) and cyclic stability (e.g. 91.6% retention after even 40,000 cycles at 50 mA cm^{-2}). An N-RGO-CNT-CBNP-P based FSSSC displays both high energy density and power density, while satisfying operational reliability/durability requirements. The results indicate that the N-RGO-CNT-CBNP-P based FSSSCs hold promise towards their practical applications for wearable electronics.

1 Introduction

Nowadays, diverse wearable electronics (e.g. bendable smartphones, rollable displays, wearable smart watches/bracelets, electronic skins, on-body biosensors and implantable medical devices) are widely pervading in human's daily life. However, ever-emerging new products or ideas have put forward severe challenges to capabilities of the current available power-supply units.[1] Conventional power devices are generally bulky, heavy and rigid, with short maintenance intervals. These inevitable drawbacks make them unable to match the requirements of future wearable electronics, such as better conformability/durability, being smaller/lighter/thinner and less/free of maintenance.[1] In the past decade, intensive research efforts have been devoted to developing advanced wearable power devices.[2] Among them, flexible solid-state supercapacitors (FSSSCs) have received extensive attention, owing to their remarkable flexibility, excellent thinness/lightness, higher power densities than those of batteries, higher energy densities than those of electrolytic capacitors, fast charge-discharge rate, superior

durability and high operation safety.[2,3]

Nanocarbons have constituted a fascinating family of nanostructured materials for energy conversion and storage.[4,5] A number of nanocarbons with diverse structural characteristics have been explored as supercapacitor electrode materials.[4] Nanocarbon supported supercapacitors store energy mainly by electrical double layer capacitance (EDLC), which arises from the formation of an electrical double layer upon the polarization effect of an electrode-electrolyte interface that is affected by an applied external voltage.[6] The accumulation of positive/negative ions onto the electrode surfaces with opposite charges can lead to charge separation rapidly and reversibly. In recent years, many pseudocapacitive materials (e.g. metal oxides, metal sulfides, metal hydroxides, and conductive polymers) have also been intensively investigated, some of which can exhibit higher specific capacitances than those of nanocarbons, but their limited cyclic stability is a serious drawback.[7] Furthermore, nanocarbons can offer many incomparable virtues for fabricating supercapacitors, such as excellent power density, remarkable cyclic stability, low cost and desirable safety/eco-friendliness.[4-6]

Among various nanocarbons, graphene nanosheets, constituted by sp^2-hybridized carbon atoms arranged in a two-dimensional (2D) monolayer structure, have been regarded as one of the most attractive representatives.[8] Theoretically, completely exfoliated and isolated graphene nanosheets can exhibit an ultrahigh specific surface area of 2630 m^2 g^{-1} and a specific capacitance of ~21 μF cm^{-2} (i.e. ~550 F g^{-1}) if their entire surface area can be fully utilized.[6] Graphene nanosheets also possess extremely high intrinsic

[a.] Department of Chemistry, Technical University of Denmark, DK-2800 Kongens Lyngby, Denmark. *E-mail: cq@kemi.dtu.dk

[b.] Department of Materials Science and NanoEngineering, SDU & Rice Joint Center for Carbon Nanomaterials, Rice University, Houston, TX 77005, USA. *E-mail: jlou@rice.edu

† Electronic Supplementary Information (ESI) available: the detail of experiments and supporting data including both spectroscopic and electrochemical data. See DOI: 10.1039/x0xx00000x

ARTICLE

mechanical strength, large lateral size, superior electric conductivity, outstanding flexibility and excellent physicochemical stability, which make them very favorable as a supercapacitor electrode material. [6,8] Chemosynthetic reduced graphene oxide (RGO) nanosheets, which are an analogue of perfect graphene nanosheets, have been widely used as an alternative for the large-scale fabrication of FSSSCs, owing to their low cost and good solution processability.[2] Even so, when practically developing RGO based paper-like FSSSC electrodes, achieving an optimal bulk density is a very crucial issue.[9] On one hand, maintaining a relatively low RGO bulk density in these electrodes is beneficial to taking full advantage of the large surface area of RGO and achieving a high mass specific capacitance. However, these could be at the expense of a low areal specific capacitance and a low macroscopic mechanical strength, which are quite unfavorable in FSSSC design. On the other hand, increasing RGO bulk density by close-packing can effectively improve their areal specific capacitance. Nevertheless, over-close-packing RGO will cause severe RGO restacking and huge loss of its effective surface areas, thereby hindering ion diffusion and inevitably resulting in capacitance attenuation and power performance degradation.

An effective countermeasure is to introduce zero-dimensional (0D) or one-dimensional (1D) nanomaterials as spacers to prevent RGO from restacking and optimize electrode micro-/nanostructures.[10] Meanwhile, these spacers are also expected to be capable of contributing additional capacitances. In previous reports, biomacromolecule and ion liquid based spacers were used to provide moderate physical separation and structural confinement effects but only very little capacitive contribution.[11,12] Some conductive polymer nanoparticles/nanotubes or metal oxide nanorods were employed as both spacers and pseudocapacitive constituents.[13-15] However, macroscopic mechanical strength and cyclic stability of these electrode materials were proved to deteriorate rapidly and markedly. Many attempts were also made on utilizing carbon nanotubes (CNTs) or carbon black nanoparticles (CBNPs), since they could effectively adjust the interplanar spacing between RGO, bridge the defects on RGO nanosheets for electron transfer, construct a highly conductive network and enhance electrolyte wettability, thereby helping improve the comprehensive performance of RGO based paper electrodes.[16-19] In addition to exploring from the perspective of materials, some advanced processing technologies such as microfluidic spinning is also being utilized for engineering hybrid-dimensional nanocomposites with novel microstructure or macroscopic morphology to address this issue.[20]

Despite the above extensive studies, to date, jointly using 0D CBNPs and 1D CNTs as spacers to develop 2D RGO nanosheets based FSSSC composite paper electrodes has not been explored yet. To develop a hybrid-dimensional nanocarbon composite with a highly-porous three-dimensional (3D) hierarchical structure could help further achieve better pore-size distribution, electrolyte wettability, charge transport and physicochemical/mechanical stability. Although relatively low mass specific capacitance is still a drawback, this issue could be substantially overcome by using heteroatom-doped nanocarbons.[21] Rationally doping heteroatoms (represented by nitrogen) into nanocarbon lattices is capable of effectively improving specific capacitance by introducing pseudocapacitive characteristics, further enhancing electrical conductivity and electrolyte wettability, without sacrificing most of essential EDLC

characteristics such as high power density and cyclic stability.[21] Herein, we propose a novel strategy to fabricate nitrogen-doped (N-doped) hybrid-dimensional nanocarbons (N-RGO-CNT-CBNP) based paper electrodes (N-RGO-CNT-CBNP-Ps, Fig. 1A) for FSSSCs. A facile approach combining microwave-assisted solvothermal self-assembly with post-annealing was employed to prepare N-RGO-CNT-CBNP. 0D CBNPs, 1D CNTs and 2D RGO nanosheets were used together as building blocks to construct its highly-porous 3D hierarchical structure. During the self-assembly process, melamine, a low-cost organic chemical with high nitrogen content (66% by mass), was used as an excellent multifunctional additive for both structural optimization and high-level nitrogen doping (N-doping). A facile multi-step filtration process (Fig. 1B) was further exploited to fabricate sandwich-structured N-RGO-CNT-CBNP-Ps. Finally, by using polyvinyl alcohol-sulfuric acid (PVA-H_2SO_4) as a gel electrolyte, an N-RGO-CNT-CBNP-P based symmetric FSSSC was assembled with its overall performance tested and evaluated systematically.

The as-prepared N-RGO-CNT-CBNP-Ps demonstrated some critical advantages: (1) with CNTs and CBNPs as both spacers and conductive linkers between RGO nanosheets, N-RGO-CNT-CBNP exhibited greatly improved porosity and electrical conductivity; (2) in virtue of the unique interactions between melamine/melamine hydrolyzates and hybrid-dimensional nanocarbons, a highly-porous 3D hierarchical structure was constructed for N-RGO-CNT-CBNP; (3) with melamine as a highly effective N-doping source, a high N-doping level of 13.8 at.% could be achieved by N-RGO-CNT-CBNP; (4) owing to the reinforcement effects caused by the structural design and compositional optimization, the N-RGO-CNT-CBNP-Ps possessed enhanced electrochemical and mechanical performance. Thanks to these significant merits, an N-RGO-CNT-CBNP-P based FSSSC could exhibit ultrahigh areal specific capacitance, excellent cyclic stability, remarkable rate capability, superior energy density and ultrahigh power density. Meanwhile, it could even maintain good supercapacitive performance under repeated bending deformation, indicating its great potential for practically powering diverse wearable electronics.

2 Experimental

2.1 Preparation of N-RGO-CNT-CBNP

In a typical experiment, activated CNTs (10 mg), activated CBNPs (10 mg), melamine (210 mg) and ethylene glycol (5 mL) were added into graphene oxide aqueous suspension (10 mL, 4 mg mL^{-1}). The suspension was ultrasonicated and stirred for 1 h to obtain a homogeneous mixture. Then, the mixture was transferred into a microwave reaction vessel with a 50% volume filling rate, and treated by a stepwise microwave-assisted solvothermal process (1st: 95 °C, 1 h; 2nd: 160 °C, 3 h). After that, the obtained product was washed, freeze-dried and annealed at 800 °C for 1 h under argon protection to obtain N-RGO-CNT-CBNP. For comparison, other nanocarbon composites including a ternary RGO-CNT-CBNP composite (w:w:w=4:1:1), a binary RGO-CNT composite (w:w=2:1) and a binary RGO-CBNP composite (w:w=2:1) as well as pure RGO were also synthesized by referring to the above procedure.

2.2 Fabrication of N-RGO-CNT-CBNP-Ps

Pure N-RGO-CNT-CBNP films obtained by filtration were very fragile

Journal Name

under strain and incapable of being directly used as flexible electrodes. Therefore, N-RGO-CNT-CBNP-Ps with a unique sandwich structure were proposed in our study, which comprising one interlayer of N-RGO-CNT-CBNP as the high-performance supercapacitive material, and two capping layers (bottom and top layers) of a RGO and CNT composite (w:w=2:1) to provide enhanced mechanical strength, flexibility, contact conductivity and electrolyte wettability (Fig. 1A). The whole process for fabricating sandwich-structured N-RGO-CNT-CBNP-Ps (Fig. 1B) was performed under room temperature and in air. To fabricate an N-RGO-CNT-CBNP-P, graphene oxide aqueous suspension (0.83 mL, 4 mg mL^{-1}), activated CNTs (1.67 mg), water (1.67 mL) and ethanol (2.5 mL) were first mixed and filtrated under 0.1 atm to obtain the bottom layer. Then, N-RGO-CNT-CBNP (20 mg) dispersed in a water-ethanol mixture (10 mL, v:v=3:1) was added onto the dried bottom layer and filtrated under 0.4 atm to produce the interlayer. After that, graphene oxide aqueous suspension (0.83 mL, 4 mg mL^{-1}), activated CNTs (1.67 mg), water (1.67 mL) and ethanol (2.5 mL) were mixed and added onto the dried interlayer and filtrated under 0.7 atm to obtain the top layer. During the processes to produce the bottom layer/interlayer, when no macroscopic liquid was left on the surface of the bottom layer/interlayer, negative pressure was continued for another 12 h. However, during the process to produce the top layer, when no macroscopic liquid was left on the surface of the top layer, negative pressure was stopped immediately and the N-RGO-CNT-CBNP-P was left to dry naturally for 24 h. Finally, the N-RGO-CNT-CBNP-P was split off from the membrane disc filter and annealed at 190 °C for 15 min in air. For evaluating the structural design of paper electrodes and calculating mass specific capacitance, a paper electrode composed of only two capping layers of the RGO and CNT composite (denoted as GC-Blank-P), a paper electrode composed of only two capping layers of pure RGO (denoted as G-Blank-P), and a paper electrode comprising one interlayer of N-RGO-CNT-CBNP and two capping layers of pure RGO (denoted as G-N-RGO-CNT-CBNP-P) were fabricated by referring to the above procedure. For comparing N-RGO-CNT-CBNP with other nanocarbon composites, sandwich-structured paper electrodes using RGO-CNT-CBNP, RGO-CNT, RGO-CBNP or pure RGO (denoted as RGO-CNT-CBNP-P, RGO-CNT-P, RGO-CBNP-P and RGO-P, respectively) as the interlayer material were also prepared via replacing N-RGO-CNT-CBNP in the N-RGO-CNT-CBNP-P structure by the same amount of other materials, respectively.

2.3 Electrochemical evaluation

All the electrochemical measurements were carried out at room temperature with argon as protective gas. Cyclic voltammetry (CV) and galvanostatic charge-discharge (GCD) tests were performed on a CHI 760C electrochemical workstation (CH Instruments). Electrochemical impedance spectroscopy (EIS) was investigated with an AUTOLAB PGSTAT12 potentiostat/galvanostat electrochemical system (Metrohm). A three-electrode set-up was used for the electrochemical evaluation of different paper electrodes. A saturated calomel electrode (SCE), a coiled platinum wire and different paper electrodes were used as the reference electrode, the counter electrode and the working electrodes respectively. Previous studies have shown that an acidic condition is more favorable for redox reactions of doped nitrogen atoms, thus 1 M H$_2$SO$_4$

was used as the electrolyte. Working electrodes were prepared with a unified structure (Fig. S1†), whose fabrication process is introduced in detail in the supplementary information. All working electrodes were immersed in 1 M H$_2$SO$_4$ for 12 h prior to use.

2.4 Fabrication and performance test of N-RGO-CNT-CBNP-P based FSSSCs

To evaluate the potential practicability of N-RGO-CNT-CBNP-Ps, using two N-RGO-CNT-CBNP-Ps and the PVA-H$_2$SO$_4$ gel electrolyte, a symmetric N-RGO-CNT-CBNP-P based FSSSC was further fabricated. Prior to fabrication, two N-RGO-CNT-CBNP-Ps were suitably tailored into a desired shape. Then moderate amounts of the PVA-H$_2$SO$_4$ gel electrolyte was uniformly smeared onto one side of the N-RGO-CNT-CBNP-Ps, which could be repeated for several times to ensure the smeared side was thoroughly wetted for 12 h. After that, the two N-RGO-CNT-CBNP-Ps were naturally dried for 6 h to vaporize excess water. Finally, with their electrolyte-smeared sides face-to-face, the two N-RGO-CNT-CBNP-Ps were pressed together for 1 h under 5 kPa to finally obtain an N-RGO-CNT-CBNP-P based FSSSC, whose overall performance was further analyzed by CV, GCD and actual power-supply tests using a two-electrode set-up.

3 Results and discussion

3.1 Synthesis and characterization of materials

3.1.1 Nanocarbons

Adopting appropriate processing and pretreatments on the three pristine nanocarbons to obtain an oxidized hybrid-dimensional nanocarbon mixture (O-RGO-CNT-CBNP) plays a key role in constructing the highly-porous and interconnected 3D network of N-RGO-CNT-CBNP. Surface functional groups of pristine CNTs and CBNPs such as carboxyl, hydroxyl and carbonyl groups could be significantly enriched after acid activation.[22,23] On the other hand, moderate addition of ammonia during the liquid-phase exfoliation of graphite oxide could help significantly improve exfoliation efficiency and achieve a more stable and dispersive graphene oxide aqueous suspension.[24] All of above are very conducive to the microwave-assisted solvothermal self-assembly of O-RGO-CNT-CBNP and finally obtaining high-quality N-RGO-CNT-CBNP.

After processing and pretreatments, the obtained graphene oxide aqueous suspension had a dark yellow color, while aqueous suspensions of both activated CNTs and activated CBNPs appeared black (Fig. S2A†). Strong characteristic absorption peaks around 220-230 nm are observed in ultraviolet-visible (UV-Vis) spectra of all the three oxidized nanocarbons, which correspond to the π-π* transition of C=C.[25] Besides, for different oxidized nanocarbons, there are also relatively weak shoulder peaks existing around 260-320 nm attributed to n-π transition of C=O in carboxyl and carbonyl groups.[26] Fourier transform infrared spectroscopy (FTIR) was used for further analyzing surface functional groups (Fig. S2B†). For all types of oxidized nanocarbons, strong characteristic absorption bands around ~3420 cm^{-1} and small shoulder peaks at ~1730 cm^{-1} are observed. The former is attributed to O–H stretching in carboxyl and hydroxyl groups, and the latter represents C=O stretching in carboxyl

ARTICLE

Journal Name

and carbonyl groups.[27] Besides, multiple peaks appearing in the range of 1300-850 cm^{-1} can be assigned to C−O stretching in various oxygen-containing groups, such as carboxyl, phenolic/alcoholic hydroxyl, ether and epoxy groups.[27] Furthermore, peaks distributing in the range of 1640-1560 cm^{-1} can be ascribed to C=C stretching in the carbon skeletons of different oxidized nanocarbons.[27] From these spectral results, it can be concluded that rich oxygen-containing groups (especially carboxyl and carbonyl groups) were introduced onto the surface of O-RGO-CNT-CBNP after the aforementioned processing/pretreatment procedures. In the meantime, the carbon skeletons in different oxidized nanocarbons could largely maintain their structural integrity.

The morphology and size of different oxidized nanocarbons are characterized and shown in Fig. S3†. From the transmission electron microscopy (TEM) images (Fig. S3A†, left), it can be seen that single layered graphene oxide nanosheets with a lateral size of 1-3 μm were successfully prepared. Rough edges and abundant surface wrinkles of graphene oxide nanosheets could be beneficial for further synthesis by exposing more oxygen-containing active functional groups.[10] A well-defined tubular structure of activated CNTs is observed (Fig. S3A†, middle). The average outer diameter of activated CNTs slightly increased to ∼10 nm, compared with that of CNTs used as starting material (∼8 nm). This could be because acid activation partially changed the outer layers of CNT sidewalls, accompanied with introducing oxygen-containing functional groups. The similar phenomenon also occurred on activated CBNPs, which were uniform spherical particles with an average diameter of ∼23 nm (Fig. S3A†, right), slightly larger than that of pristine CBNPs (∼20 nm). The atomic force microscopy (AFM) image further supported that the obtained graphene oxide were mainly single-layered nanosheets with a thickness of around 0.85 nm (Fig. S3B†, left). For pristine and activated CNTs, there were no significant morphology difference observed (Fig. S3B†, middle and right). Their diameters were measured to be ∼8 nm and ∼11 nm as expected, respectively, which further validates the above-mentioned acid activation induced size variation. The minimal dispersible structural unit of carbon black is generally a multi-core aciniform aggregate composed of dozens of randomly-arranged CBNPs fused together.[28] Besides, small CBNP aggregates tend to clump and agglomerate into larger aggregates during sample-drying processes. Thus, it was unable to observe the size of every individual CBNP by AFM. However, dynamic light scattering (DLS) can be employed to directly investigate the actual size distribution of CBNP aggregates in the adopted solvent (Fig. S3C†). It can be seen that the average size of CBNP aggregates increased from ∼140 nm to ∼190 nm after acid activation. It could be attributed to the successful introduction of abundant surface hydrophilic groups, which increased both the actual and the hydrodynamic size of CBNP aggregates.[29] Moreover, no giant CBNP aggregates (diameter > 800 nm) were observed after acid activation. All above results confirm that the structures and physical characteristics of as-prepared nanocarbons were adequately tailored for the synthesis of N-RGO-CNT-CBNP.

3.1.2 N-RGO-CNT-CBNP

A variety of nanocarbons are found to be excellent microwave absorbents.[30] Owing to their ultra-active interactions with microwave radiation, fast, violent and heterogeneous heating can be realized, enabling the acceleration of reaction processes, as well as the formation of innovative nanocarbon-based composites/structures with unusual morphologies.[30,31] The specific strategy for synthesizing N-RGO-CNT-CBNP is illustrated in Fig. 2 and the structure characterization of N-RGO-CNT-CBNP will be described in detail below. Considering the discrepant water solubility/dispersity of starting materials and the superior microwave absorption ability of polyols, a binary mixture of water and ethylene glycol was employed as the solvent, by which a homogeneous dispersion was obtained for the following microwave processing (Fig. 2A). In the first stage (Fig. 2B), melamine began to hydrolyze into different hydrolyzates (Fig. S4A†) under the acidic environment caused by the abundant carboxyl groups of O-RGO-CNT-CBNP.[32] Small molecular clusters composed of melamine and its hydrolyzates (especially its tertiary hydrolyzate, cyanuric acid) rapidly formed via strong hydrogen bonding (Fig. S4B and S4C†).[33,34] Meanwhile, many melamine/melamine hydrolyzate molecules could be closely adsorbed or chemically bonded onto the surface of O-RGO-CNT-CBNP.[35,36] In the second stage (Fig. 2C), melamine and its primary hydrolyzates further hydrolyzed with increasing temperature. A supramolecular prismatic structure was constructed by the rapid self-assembly of small molecular clusters produced in the first stage. Owing to its self-protecting effect, these microprisms could keep stable and growing, and function with CNTs and CBNPs together as highly effective spacers to prevent RGO nanosheets from restacking, thereby producing the melamine/melamine hydrolyzates loaded RGO-CNT-CBNP composite (M-RGO-CNT-CBNP) with a 3D highly-porous and interconnected network structure. During microwave processing, with melamine as primary nitrogen source, initiatory N-doping of nanocarbons was also realized by making use of the nanoscale localized instantaneous super-heating effects.[31] It was reported that partially oxidized areas on nanocarbons with sufficient nitrogen source molecules adsorbed/conjugated could absorb microwave intensively.[37] Under microwave irradiation, these areas were superheated with generated heat rapidly dissipated to hydrophilic oxygen-containing groups by π electron migration. After that, with deoxygenation occurring, many nitrogen atoms generated by the decomposing of nitrogen source molecules could be doped into the lattices of nanocarbons efficiently.[37] Following the solvothermal self-assembly process, a post-annealing treatment was adopted to simultaneously realize higher-level thermal reduction and N-doping of nanocarbons. This process also occurred in two stages. First, adsorbed melamine and its derivatives began to condense to graphitic carbon nitride (g-C_3N_4) when the annealing temperature rised to 500-650 °C (Fig. 2D).[38] Remaining oxygen-containing groups were then removed rapidly from the surface of nanocarbons, creating abundant active sites for N-doping. In the second stage, with the annealing temperature further increasing to 650-800 °C (Fig. 2E), nitrogen free radicals as well as some other nitrogen-containing species formed by decomposition of g-C_3N_4 could attack these active sites to form N-RGO-CNT-CBNP.[38]

X-ray powder diffraction (XRD) was used for identifying atomic-level structural changes of N-RGO-CNT-CBNP before and after synthesis (Fig. 3A). From curve (1), it is shown that all main diffraction peaks of three oxidized nanocarbons can be observed clearly, which means they were adequately activated and homogenously mixed for further self-assembly. A series of sharp peaks are detected in curve

(2) from 10° to 40°, which are in good agreement with those of previously reported crystalline melamine (JCPDS: 39-1950).[39] From curves (3) and (4), it can be seen that after solvothermal processing and annealing treatment, a strong diffraction peak appears around 24.9°, which can be attributed to enhanced characteristic diffraction of graphitic (002) planes in reduced nanocarbons. The strong diffraction peak at 11.4° corresponding to the (001) plane of graphene oxide totally disappeared in curve (3) and (4), indicating the high reduction degree of reduced nanocarbons. The characteristic diffraction peaks of melamine does not exist in curve (4), suggesting its complete decomposition. The high similarity of curve (3) and (4) indicates N-RGO-CNT-CBNP could still retain a relatively stable carbon skeleton like RGO-CNT-CBNP. Besides, compared with those of RGO-CNT-CBNP, the (002) and (100) peaks of N-RGO-CNT-CBNP are relatively stronger and broader. This could be due to the changes in lattice orientations derived from both the introduced defects and the highly-porous structure of N-RGO-CNT-CBNP.

Raman spectroscopy was employed for further microstructural analysis. As shown in Fig. 3B, the Raman spectra of different nanocarbon composites exhibited two prominent peaks around 1345 and 1580 cm^{-1}, which corresponds to D band and G band of graphitic structures, respectively. The G band corresponds to the in-plane bond-stretching of sp^2-bonded graphitic structures, while the D band is associated with structural disorder induced scattering derived from lattice imperfections and symmetry deficiencies of sp^2-bonded graphitic structures.[40] From curve (1) and (4), it can be seen that after reduction, the peak intensity ratio of D band to G band (I_D/I_G) increased from 0.85 for O-RGO-CNT-CBNP to 1.19 for RGO-CNT-CBNP, which may be because the removal of oxygen-containing groups induced smaller and more dispersed sp^2 domains, thereby leading to more defects in the sp^2-bonded graphitic structures. While introducing melamine (curve (3)), it can be seen that several characteristic peaks stemming from melamine exist in the range of 550-1050 cm^{-1}, indicating there was still a high content of melamine and its hydrolyzates in M-RGO-CNT-CBNP for structure adjustment and high-temperature N-doping. Besides, compared with curve (1), the D band intensity of M-RGO-CNT-CBNP significantly increases with the I_D/I_G value rising up to 1.71. This could be because the adsorbed/conjugated nitrogen-containing species in M-RGO-CNT-CBNP created more lattice defects and distortion in graphitic structures of nanocarbons. After thermal reduction of M-RGO-CNT-CBNP, the I_D/I_G value decreased to 1.32 (curve (5)). Meanwhile, the characteristic peaks of melamine and melamine hydralyzates in curve (3) disappeared in curve (5). These phenomena suggest the complete transformation of all adsorbed/conjugated nitrogen-containing species. Furthermore, compared with curve (4), the relatively higher I_D/I_G value as well as the presence of a small shoulder peak around 1620 cm^{-1} (D') in N-RGO-CNT-CBNP indicate the high-level N-doping has introduced abundant symmetry-breaking structural defects. However, it should be noted that the G band of N-RGO-CNT-CBNP still possesses high similarity with that of RGO-CNT-CBNP, which indicates a relatively stable graphitic structure has been largely retained.

Thermogravimetric analysis (TGA) was used for investigating the relationship between micro-/nanoscopic structure and thermal stability of N-RGO-CNT-CBNP. As shown in Fig. 3C, pristine graphite

powder exhibited no obvious weight loss up to 650 °C. Further increasing the temperature resulted in the rapid pyrolysis of its graphitic skeleton. O-RGO-CNT-CBNP started to continuously loss weight from the very beginning due to the gradual deprivation of trapped moistures. A rapid weight loss occurred from 180 to 300 °C, which could be attributed to the decomposition of various oxygen-containing groups. The graphitic skeleton of O-RGO-CNT-CBNP started to decompose from only about 520 °C, which may due to its greatly reduced van der Waals interactions and significant self-catalytic effect. Compared with the 56% weight loss of O-RGO-CNT-CBNP at 520 °C, RGO-CNT-CBNP and N-RGO-CNT-CBNP achieved much lower weight losses of 16% and 21%, respectively, indicating their high reduction degree. Their graphitic skeleton started to be pyrolysed from more than 550 °C, which may because the tandem microwave-thermal reduction process helped optimize the microstructure of graphitic skeletons and enhanced their thermal stability. Interestingly, it was found that N-RGO-CNT-CBNP were even more thermally stable than RGO-CNT-CBNP under 650-750 °C, which could be ascribed to the introduced nitrogen-containing heterocyclic rings can further restore and reinforce its graphitic skeleton, thereby achieving a better thermal stability.

X-ray photoelectron spectroscopy (XPS) was used for further analyzing elemental compositions and nitrogen bonding states of N-RGO-CNT-CBNP. In Fig. 4A, the XPS survey spectra showed that compared with that of O-RGO-CNT-CBNP, the oxygen contents in RGO-CNT-CBNP and N-RGO-CNT-CBNP decreased significantly after reduction, demonstrating the proposed synthetic approach could help O-RGO-CNT-CBNP achieve a high reduction degree. Besides, compared with that of RGO-CNT-CBNP, the intensity of O1s in N-RGO-CNT-CBNP decreased by extra 16%, which indicates the introduction of melamine could further promote the reduction of oxygen-containing groups, realizing highly-efficient N-doping simultaneously. A high N-doping level of 13.8 at.% could be achieved by N-RGO-CNT-CBNP, demonstrating that melamine could function as a highly effective N-doping source. In Fig. 4B, the N1s spectrum of N-RGO-CNT-CBNP can be fitted into four peaks with binding energies of 398.2 (pyridinic nitrogen), 400.4 (pyrrolic nitrogen), 401.7 (graphitic nitrogen) and 403.8 eV (pyridinic-oxide nitrogen), respectively. Previous studies have demonstrated that for N-doped carbon materials, pyridinic nitrogen and pyrrolic nitrogen are predominant electrochemical redox active sites for efficiently providing pseudocapacitance.[41] It is shown that the proportion of pyridinic nitrogen and pyrrolic nitrogen in the total doped nitrogen content of N-RGO-CNT-CBNP was higher than 85%. This result indicated that by using melamine as an efficient nitrogen source and employing our unique reaction approach, both a high nitrogen doping level and favorable nitrogen doping types could be achieved simultaneously by N-RGO-CNT-CBNP.

TEM and scanning electron microscopy (SEM) were employed for investigating micro-/nanoscopic morphologies of N-RGO-CNT-CBNP. In Fig. 5, RGO nanosheets, CNTs and CBNPs can be respectively observed in both RGO-CNT-CBNP and N-RGO-CNT-CBNP. However, it can be clearly seen that there were many isolated CNT or CBNP conglomerations and uncombined RGO nanosheets existing in RGO-CNT-CBNP, indicating its poor material homogeneity (Fig. 5E-5H). By contrast, a more uniform material distribution was achieved by N-RGO-CNT-CBNP at even nanoscale (Fig. 5A-5D). This could be

because during the solvothermal self-assembly, by the efficient adsorption/conjugation of melamine and its hydrolyzates, relatively hydrophobic and chemically-inert basal planes of nanocarbons (especially RGO) could be significantly 'activated'. Functioning as linker molecules (Fig. 2B), melamine and its hydrolyzates greatly prompted homogenization and recombination of different nanocarbons. The as-achieved better homogeneity of N-RGO-CNT-CBNP was very beneficial to taking full advantages of all nanocarbons working in different dimensions. On the other hand, by the synergetic effect of CNT/CBNP spacing and melamine-mediated microstructure directing, more wrinkles were produced onto RGO nanosheets, which could effectively prevent RGO restacking and introduce plentiful nano-/mesopores (Fig. 5A and 5C). Besides, it can be seen that many microprisms composed of melamine and its hydrolyzates existed in M-RGO-CNT-CBNP (Fig. S5†). These microprisms themselves could also serve as highly effective spacers capable of providing robust spatial supports at microscale. Although the microprisms were decomposed after thermal annealing, the high temperature graphitization of g-C$_3$N$_4$ could produce a reinforcing effect on the structural junctions of hybrid-dimensional nanocarbons. Therefore, the highly-porous 3D hierarchical structure was furthest retained in N-RGO-CNT-CBNP, and abundant macropores were also created which could further enhance electrolyte transport (Fig. 5C). In addition, an energy-dispersive X-ray spectroscopy (EDX) analysis was conducted to observe the elemental composition of N-RGO-CNT-CBNP (Fig. S6†). The obtained results were largely consistent with those we got from XPS analysis, which could also demonstrate the high compositional homogeneity of N-RGO-CNT-CBNP considering the dissimilar observed emphases of the two techniques.

Nitrogen adsorption-desorption isotherms were used for further analyzing the specific surface area and porosity of N-RGO-CNT-CBNP. In Fig. 6A, all isotherms exhibit type-IV features with evident type-H3 hysteresis loops in the medium and high relative pressure range (> 0.4) and steep uptakes in the low relative pressure range (<0.01), revealing the coexistence of micropores, mesopores and macropores in corresponding nanocarbon composites. Compared with that of O-RGO-CNT-CBNP, the specific surface area of RGO-CNT-CBNP increased by ~60%, which could be because the reduction and drying processes were capable of releasing some suppressed micropores and small mesopores in O-RGO-CNT-CBNP. On the other hand, the specific surface area of M-RGO-CNT-CBNP was almost three times that of O-RGO-CNT-CBNP, and a greatly enhanced overall porosity was achieved by M-RGO-CNT-CBNP (Fig. 6B). These could be because the introduction of melamine helped achieve a more homogenous distribution of different nanocarbons, and the integrated spacing effect derived from both CNTs/CBNPs and melamine based microprisms could effectively hinder RGO restacking and construct a highly-porous 3D hierarchical structure. Although having undergone further thermal reduction, a high specific surface area of 810 m^2 g^{-1}, a large total pore volume of 3.32 cm^3 g^{-1} and a large average pore diameter of 16.4 nm could be still achieved by N-RGO-CNT-CBNP, indicating the highly-porous 3D hierarchical structure of M-RGO-CNT-CBNP was largely retained. Compared with that of M-RGO-CNT-CBNP, the slight loss (~12%) of the specific surface area of N-RGO-CNT-CBNP was mainly attributed to the amount decrease of pores with a size of 8-50 nm. This could be due to the complete thermal

decomposition of melamine based microprisms, which might induce the partly collapse of their attached nanostructures constructed by CNTs and CBNPs.

3.1.3 N-RGO-CNT-CBNP-P

The morphology and microstructure of sandwich-structured N-RGO-CNT-CBNP-Ps was investigated. Fig. 7A shows a typical circular N-RGO-CNT-CBNP-P with a diameter of ~4 cm, exhibiting its free-standing and flexible feature. From Fig. S7†, it can be seen that the N-RGO-CNT-CBNP-P could be folded/unfolded for several times without apparent damage, further demonstrating its excellent flexibility. Fig. 7B show the cross-sectional image of a ~10 μm thick N-RGO-CNT-CBNP-P, whose interlayer and capping layers are ~8 and ~1 nm thick, respectively. Compared with the interlayer, the capping layers were more compact with RGO nanosheets and CNTs uniformly stacking on each other. The introduction of CNTs were capable of providing enhanced mechanical protection to the interlayer and further improving surface electrical conductivity. Their spacing effect could also help facilitate electrolyte transport. From Fig. 7C, it can be seen that in spite of undergoing a negative-pressure filtration process, the microstructure of N-RGO-CNT-CBNP could be largely retained. The abundant hierarchical pores and highly interconnected 3D conductive network in the interlayer is very conducive to improving the EDLC-type energy storage capacity of N-RGO-CNT-CBNP-Ps.

The macroscopic electrical and mechanical properties of different papers were then comprehensively evaluated. The electrical conductivity of different papers are shown in Table S1†. Compared with that of a G-N-RGO-CNT-CBNP-P, an N-RGO-CNT-CBNP-P could achieve a higher surface electrical conductivity, since the introduced CNTs in the capping layer could serve as highly conductive 'bridges' among RGO nanosheets. The cross-plane electrical conductivity of different papers were also measured. Attributed to the synergistic effect of the electron transport 'highways' constructed by highly conductive spacers and the improved intrinsic electrical conductivity owing to effective N-doping, N-RGO-CNT-CBNP-Ps could achieve the highest cross-plane electrical conductivity. Fig. S8† shows the stress-strain curves of different papers. Listed in Table S2†, the calculated Young's modulus of different papers varied from 5-10 GPa with a RGO-P achieving the highest value owing to its higher RGO content. It could be seen that in spite of its relatively low RGO content, an N-RGO-CNT-CBNP-P could withstand a highest stress of 200 MPa with 2.56% tensile strain among the measured samples, with its stiffness largely retained. On one hand, it is owing to the superior mechanically reinforcing effect of the introduced CNTs and CBNPs, which could bridge RGO nanosheets and effectively resist the functional failure induced by structural deformation. On the other hand, it benefited from the microwave super-heating effect, by which RGO nanosheets, CNTs and CBNPs could be effectively 'welded' together with the aid of the adsorbed melamine-containing supramolecules (Fig. 2C). Therefore, the 3D hierarchical nanocarbon network of the N-RGO-CNT-CBNP-P could be further reinforced, and its higher structural integrity were capable of effectively resisting tensile deformation. Fig. S9A† shows the impacts of tensile and bending strain on the electrical conductivity of an N-RGO-CNT-CBNP-P. With the tensile strain increasing, surface electrical conductivity of the N-RGO-CNT-CBNP-P

tended to decrease due to the weakened interconnection among RGO nanosheets. However, surface electrical conductivity decrease of the N-RGO-CNT-CBNP-P was still less than 5% even when tensile strain was as high as 1.5%, owing to the bridge effect of CNTs and CBNPs. Meanwhile, cross-plane electrical conductivity of the N-RGO-CNT-CBNP-P slightly increased, which could be ascribed to the improved compactness in the cross-plane direction. A bending fatigue test was also conducted for an N-RGO-CNT-CBNP-P. The N-RGO-CNT-CBNP-P showed no obvious appearance change even after 10,000 repeated bending-unbending cycles, with the loss of both the surface and the cross-plane electrical conductivity less than 3% (Fig. S9B†). These results demonstrated superior macroscopic electrical and mechanical characteristics of the N-RGO-CNT-CBNP-P.

3.2 Electrochemical evaluation of electrode materials and flexible electrodes

As discussed above, both the highly-porous 3D hierarchical structure and the optimized N-doping of N-RGO-CNT-CBNP as well as the unique sandwich-structured configuration endowed N-RGO-CNT-CBNP-Ps with great potential for supercapacitive energy storage. Fig. 7D shows the CV curves of different paper electrodes at a scan rate of 5 mV s^{-1}. It is observed that the CV curve of a GC-Blank-P is approximately rectangular with no apparent redox peaks, showing a typical characteristic of ideal EDLC. After introducing different interlayer materials (pure RGO, RGO-CBNP, RGO-CNT and RGO-CNT-CBNP) into GC-Blank-Ps, a pair of broad but weak redox peaks emerge around 0.5-0.6 V due to the redox reactions of their residual surface oxygen-containing groups.[42] Current densities of corresponding paper electrodes (the RGO-P, RGO-CBNP-P, RGO-CNT-P and RGO-CNT-CBNP-P) also increased and the RGO-CNT-CBNP-P could achieve a relatively high current response. Since the amounts of interlayer materials in all the sandwich-structured paper electrodes were the same, it could be demonstrated that introducing CNTs and CBNPs jointly and adopting an optimal weight ratio of three nanocarbons (RGO:CNT:CBNP=4:1:1) were conducive to restraining RGO restacking and retaining their large specific surface area, thereby helping the RGO-CNT-CBNP-P achieve a higher EDLC.

Before focusing on the electrochemical performances of N-RGO-CNT-CBNP-Ps, the effect of adopting different key reaction parameters on the N-doping level and the supercapacitive performance of N-RGO-CNT-CBNP has been preliminarily investigated. The impact of adjusting the added amount of melamine on the overall nitrogen content and the mass specific capacitance of N-RGO-CNT-CBNP was first investigated (Fig. S10†). While the mass ratio of melamine to three nanocarbons was in the range of (0.5~3.5):1, both the overall nitrogen content and the mass specific capacitance of N-RGO-CNT-CBNP increased with gradually increasing the added amount of melamine, which validated that a relatively high N-doping level was conducive to helping N-RGO-CNT-CBNP achieve a better supercapacitive performance. However, while the weight ratio exceeded 3.5:1, there was no further obvious increase of the overall nitrogen content of N-RGO-CNT-CBNP. Besides, the mass specific capacitance of N-RGO-CNT-CBNP even slightly decreased, which might be because the excessive addition of melamine into the reaction mixture will impair the structural continuity and stability of N-RGO-CNT-CBNP, thus resulting in structural degradation and restrained electron transfer in N-RGO-

CNT-CBNP during electrochemical measurements.[20] Furthermore, differing from many classical points of view concluding that N-doping induced supercapacitive performance improvements could be mainly attributed to pyridinic and pyrrolic type N-doping, through the process of optimizing thermal annealing parameters (Table S3†), we found that when the overall N-doping reached a high level, a relatively low ratio of pyridinic and pyridinic-oxide nitrogen could instead help nanocarbons achieve better supercapacitive performance, since higher electrical conductivity could be achieved.[20]

When using the optimizedly synthesized N-RGO-CNT-CBNP as an interlayer material, it can be seen that two pairs of apparent redox peaks can be found in the CV curve of an N-RGO-CNT-CBNP-P, which could be attributed to the redox activities of pyridinic and pyrrolic nitrogen, respectively.[43] It can be clearly observed that the N-RGO-CNT-CBNP-P could achieve the highest current response among all the paper electrodes. On one hand, compared with RGO-CNT-CBNPs, the further optimized micro-/nanostructure, increased specific surface area and improved electrolyte wettability of N-RGO-CNT-CBNPs could benefit the N-RGO-CNT-CBNP-P possessing a higher EDLC. On the other hand, a high pseudocapacitance could be simultaneously achieved owing to the active redox behaviors of optimizedly-doped nitrogen atoms in N-RGO-CNT-CBNPs. Their effective combination endowed the N-RGO-CNT-CBNP-P with greatly enhanced capability for supercapacitive energy storage. Fig. 7E shows the CV curves of the N-RGO-CNT-CBNP-P measured over a wide range of scan rates from 5 to 500 mV s^{-1}. It can be seen that the shape of the CV curve at a scan rate of 500 mV s^{-1} could still retain a quasi-rectangular shape with stable Faradaic peaks, suggesting that good rate performance could be achieved by the N-RGO-CNT-CBNP-P owing to its fast charge transport and ion response.

Areal specific capacitance is a key parameter for evaluating the application potential of a paper electrode for flexible energy storage. Fig. 7F shows the GCD curves of different paper electrodes at a current density of 1 mA cm^{-2}. From their discharge times, areal specific capacitances of the GC-Blank-P, RGO-P, RGO-CBNP-P, RGO-CNT-P, RGO-CNT-CBNP-P and N-RGO-CNT-CBNP-P were calculated to be 90, 286, 316, 369, 445 and 935 mF cm^{-2}, respectively. These values agreed well with the above comparison results by CV curves. Significantly, benefiting from its optimized constituents and superior structure configuration, the N-RGO-CNT-CBNP-P could achieve a much higher areal specific capacitance (Table S4†) than those of other paper electrodes as well as many reported nanocarbon based flexible electrodes,[44-47] and even comparable to those of many metal oxide or conductive polymer based flexible electrodes.[48-50] For calculating the mass specific capacitances of N-RGO-CNT-CBNP, we assumed that the capacitance of a GC-Blank-P was equal to the capacitance of the two capping layers of an N-RGO-CNT-CBNP-P, and the capacitance of an N-RGO-CNT-CBNP-P was approximatively equal to the sum of capacitances of its interlayer and capping layers (Fig. S11†). By deducting the capacitance contribution from capping layers, the mass specific capacitance of N-RGO-CNT-CBNP at 1 mA cm^{-2} (~0.4 A g^{-1}) was further calculated to be 531 F g^{-1}, which as far as we know is a record-high specific capacitance value for heteroatom-doped graphene based nanocarbon composites (Table S5†). Fig. 7G shows the GCD curves of the N-RGO-CNT-CBNP-P at different current densities. Nearly triangular GCD curves over a wide

range of current densities from 1 to even 100 mA cm^{-2} could be obtained, implying fast Faradaic reactions and remarkable rate capability of the N-RGO-CNT-CBNP-P, Moreover, almost no potential drop can be observed, suggesting that the RGO-CNT-CBNP-P possessed a quite low internal resistance. Fig. 7H shows the areal specific capacitances of different paper electrodes at different current densities. The areal specific capacitances could decrease gradually with increasing current density, which was mainly related to the influence of higher ion-diffusion resistances. It is found that the areal specific capacitances of various undoped nanocarbon based paper electrodes could retain 69%-76% with current density increasing from 1 to 100 mA cm^{-2}. Under the same condition, the areal specific capacitance of the N-RGO-CNT-CBNP-P could retain 62%, indicating that even if N-RGO-CNT-CBNP possessed a quite high N-doping level, the superior rate performance of undoped nanocarbons could be largely inherited by N-RGO-CNT-CBNP. Fig. S12† shows a comparison of cyclic stability of the N-RGO-CNT-CBNP-P, RGO-CNT-CBNP-P and RGO-P based on the results from GCD tests at a current density of 50 mA cm^{-2} (~21 A g^{-1}) for 40,000 cycles. The specific capacitance retention of 91.6%, 94.4% and 96.3% could be achieved by the N-RGO-CNT-CBNP-P, RGO-CNT-CBNP-P and RGO-P, respectively. This result indicates that the superior cyclic stability derived from EDLC characteristics of undoped nanocarbons was also greatly retained by the N-RGO-CNT-CBNP-P.

The influence of introducing CNTs into the capping layers on electrochemical behaviors of the N-RGO-CNT-CBNP-P was also investigated. From Fig. S13A†, it can be seen that at a relatively low scan rate (5 mV s^{-1}), the mass specific capacitance of N-RGO-CNT-CBNP showed only slight difference with or without the existence of CNTs in the capping layers. However, with increasing current density, the N-RGO-CNT-CBNP was capable of achieving better rate performance than the G-N-RGO-CNT-CBNP-P (Fig. S13B†). This could be because introducing CNTs into the capping layers could increase their porosity for electrolyte transport, which made N-RGO-CNT-CBNP in the interlayer more electrolyte-accessible, especially at higher current densities.

By loading different amounts of N-RGO-CNT-CBNP, the impact of regulating the thickness of an N-RGO-CNT-CBNP-P on the areal specific capacitance of the N-RGO-CNT-CBNP-P and the mass specific capacitance of N-RGO-CNT-CBNP was further studied (Fig. S14†). On one hand, the areal specific capacitance scales linearly with increasing the electrode thickness in the range of 3-12 μm. However, with further increasing the electrode thickness, the areal specific capacitance of the N-RGO-CNT-CBNP-P gradually comes to its saturated state due to its limited electrolyte infiltration. On the other hand, a higher mass specific capacitance can be achieved by N-RGO-CNT-CBNP when the electrode thickness is in the range of 3-12 μm, which could be because adopting a low loading amount of N-RGO-CNT-CBNP could help N-RGO-CNT-CBNP effectively maintain its large surface area. If further increasing the electrode thickness, an obvious decline of the mass specific capacitance could be obtained due to the close-packing effect restricting fast ion diffusion. It can be seen that a theoretical optimal electrode thickness in this study was around 13 nm and our adopted electrode thickness (~12 nm) for further fabricating FSSSCs is quite close to the theoretical optimal value. The macroscopic bulk density of N-RGO-CNT-CBNP in a ~12 nm thick N-RGO-CNT-CBNP-P was also calculated to be ~1.6 g cm^{-3}. It should be

noted when utilizing our flexible electrodes for specific applications, more factors such as electrode area and shape should be also considered and evaluated.

EIS was conducted to study the internal resistance, charge transport and ion diffusion of different paper electrodes. Fig. 7I compares the Nyquist plots of the N-RGO-CNT-CBNP-P, RGO-CNT-CBNP-P and RGO-P with the upper inset showing the equivalent circuit. The intercepts of the abscissa axis represent intrinsic ohmic resistance (R_s). The R_s values of the N-RGO-CNT-CBNP-P, RGO-CNT-CBNP-P and RGO-P are 0.37, 0.45 and 1.25 Ω, respectively. The lower intrinsic ohmic resistance of the N-RGO-CNT-CBNP-P could be because the optimizedly-doped nitrogen atoms were capable of further facilitating electron transfer. The diameters of quasi-semicircles represent charge transfer resistance (R_{ct}) originating from the electrode-electrolyte interface. The R_{ct} values of the N-RGO-CNT-CBNP-P, RGO-CNT-CBNP-P and RGO-P are 0.15, 0.24 and 0.57 Ω, respectively. The smaller R_{ct} value achieved by the N-RGO-CNT-CBNP-P indicates its fast ion response derived from the improved electrolyte wettability and enhanced ion diffusion of N-RGO-CNT-CBNP. Besides, slopes at the low frequency region represent the Warburg impedances (Z_w), which reflect electrolyte transport efficiency. It can be seen that the slope of the N-RGO-CNT-CBNP-P curve is clearly larger than those of the RGO-CNT-CBNP-P and RGO-P curves, and much closer to +∞. This superior capability for electrolyte transport could be ascribed to the highly-porous 3D hierarchical microstructure of N-RGO-CNT-CBNP.

3.3 Device performance evaluation of flexible solid-state supercapacitors

In order to evaluate actual device behaviors of the as-fabricated flexible N-RGO-CNT-CBNP-P, a two-electrode test was carried out to investigate the supercapacitive performance of an N-RGO-CNT-CBNP-P based symmetric FSSSC. The FSSSC was simply constituted by two N-RGO-CNT-CBNP-P based flexible electrodes and a PVA-H$_2$SO$_4$ gel electrolyte (Fig. 8A) with no need of any other current collector, substrate and separator. The FSSSC could be mounted onto a finger without any observable mechanical breakage. Fig. 8B shows the CV curves of the FSSSC measured at different scan rates. The CV curves display a rectangular shape with no apparent Faradaic peaks, differing from the CV curve shape of N-RGO-CNT-CBNP-Ps obtained in the three-electrode test. This is because the N-RGO-CNT-CBNP-P based electrodes in the FSSSC could be charged and discharged at a pseudo-constant rate over the entire voltammetric cycles.[51] Even at a high scan rate of 500 mV s^{-1}, the CV curve can still keep a quasi-rectangle shape, exhibiting its good rate performance. To validate its feasibility as a flexible power source, CV curves of the FSSSC under flat and bent states was measured. The CV curves show almost the same capacitive behaviors with no apparent variation at different bending angles (Fig. 8C), demonstrating that superior flexibility of the FSSSC could ensure its structural integrity and operational reliability even under bent states. GCD curves were recorded at different current densities from 1 to 100 mA cm^{-2}. As shown in Fig. 8D, all GCD curves show a symmetric triangular shape with high linearity, indicating nearly ideal capacitive characteristics of the FSSSC. The FSSSC could deliver high areal specific capacitance values of 499, 442, 396, 360, 312, 276 and 245 mF cm^{-2} at discharge current densities of 1, 2, 5, 10, 20, 50 and 100 mA cm^{-2}, respectively. The capacitance

decrease was due to the increased insufficiency of active materials used in the redox reaction when a high scan rate was adopted. Compared with the areal specific capacitance at 1 mA cm^{-2}, 49.1% of capacitance retention could be achieved at 100 mA cm^{-2}, revealing good rate performance of the FSSSC. Cyclic performance of the FSSSC was investigated by a GCD test at a current density of 50 mA cm^{-2}. As shown in Fig. 8E, the FSSSC exhibited excellent cyclic stability with a high capacitance retention of 86.5% after 30,000 charge-discharge cycles. No significant changes of electrochemical behaviors could be observed after the long-term running. In the meanwhile, the calculated Coulombic efficiency of the FSSSC was always kept in the range of 98.7%-100%, further demonstrating its superior electrochemical stability. SEM was used for observing the morphology of a cycled electrode (Fig. S15†). It can be seen that even if undergoing the high mechanical pressure during fabrication and the long-term cycling at a high current density, compared with the initial state of the N-RGO-CNT-CBNP-P shown in Fig. 7B and 7C, no apparent morphology change could be observed, and the highly-porous structure was largely retained. Fig. 8F shows the resistance of the cycled FSSSC only slightly increased with an R_{ct} of 2.16 Ω and an R_s of 1.51 Ω, compared with the uncycled FSSSC which possessed an R_{ct} of 1.75 Ω and an R_s of 1.27 Ω. Ragone plots are often used for performance comparison of various energy-storing devices. Fig. S16† shows gravimetric Ragone plots of the FSSSC and some other reported supercapacitor devices. A mass specific energy of 10.9 W h kg^{-1} at 78.5 W kg^{-1} and a mass specific power of 7856 W kg^{-1} at 5.3 W h kg^{-1} were achieved by the FSSSC. It can be seen that although a common polymer electrolyte and a simple symmetric structural configuration were used for fabricating the N-RGO-CNT-CBNP-P based FSSSC, the final power device still exhibited quite competitive power capabilities, superior to those of not only most of nanocarbon or heteroatom doped nanocarbon based supercapacitors,[44,52,53] but also even some metal oxide or conductive polymer based supercapacitors.[47,50] Areal specific energy/power could be more reasonable factors than gravimetric ones when evaluating the potential practicability of a FSSSC for wearable applications. Fig. 8G shows areal Ragone plots of the FSSSC and some other reported supercapacitor devices. An areal specific energy of 0.07 mW h cm^{-2} at 0.5 mW cm^{-2} and an areal specific power of 50 mW cm^{-2} at 0.034 mW h cm^{-2} were obtained, which were among the highest values for nanocarbon based FSSSCs recorded to date.[47,50,54-66] By a simple GCD test, we further tested the operational characteristics of multiple FSSSCs working simultaneously. The capacitance of each FSSSC unit used here was measured respectively with an initial capacitance deviation smaller than 1%. As shown in Fig. 8H, the potential window for a power device based on three series-connected FSSSCs was extended from 1 to 3 V. It can be seen that at the same current density, the charge-discharge time were essentially unchanged. Besides, with a potential window of 0-1 V, the discharge time for a power device based on three parallel-connected FSSSCs at the same current density could be nearly tripled. These results indicated the great potential of the FSSSC for being applied in complicated circuits with its capacitive performance well retained. Lastly, we used the power device based on three series-connected FSSSCs to power some small commercial electronics (Fig. 8I). The power device was capable of powering a red, blue or yellow light emitting diode (LED) whose working potentials ranging from 1.8 to 2.4 V, as well as a small

digital voltmeter, demonstrating superior practical potential of the FSSSC for flexible energy storage.

4. Conclusions

In summary, we have developed the facile synthesis of N-RGO-CNT-CBNP and used it to prepare N-RGO-CNT-CBNP-Ps with favorite structures for fabricating high-performance FSSSCs. Owing to the unique synthetic approach and the multiple beneficial effects of melamine, N-RGO-CNT-CBNP with a highly-porous 3D hierarchical structure and a high doping level (13.8 at.%) was successfully synthesized from combining three types of nanocarbons. Sandwich-structured N-RGO-CNT-CBNP-Ps were further fabricated with enhanced flexibility, conductivity and mechanical strength. Electrochemical analyses revealed that the as-synthesized N-RGO-CNT-CBNP possessed a high mass specific capacitance of 531 F g^{-1} at ~0.4 A g^{-1}, and the N-RGO-CNT-CBNP-P could achieve an ultrahigh areal specific capacitance of 935 mF cm^{-2} at 1 mA cm^{-2}, with remarkable rate capability and cyclic stability. These superior supercapacitive performance could be attributed to the optimized composition and unique structural configuration of N-RGO-CNT-CBNP-Ps. An N-RGO-CNT-CBNP-P based symmetric FSSSC could exhibit an areal specific energy of 0.07 mW h cm^{-2} at a power density of 0.5 mW cm^{-2}, remarkable cyclic stability (86.5% of capacitance retention after 30,000 charge-discharge cycles) and satisfying operational reliability, which are superior to those of most of reported FSSSCs. These fascinating results demonstrated great potential of N-RGO-CNT-CBNP-P based FSSSCs in achieving high-performance flexible energy storage for their use in advanced wearable electronics.

Conflicts of interest

There are no conflicts to declare.

Acknowledgements

References

1   A. Sumboja, J. Liu, W. G. Zheng, Y. Zong, H. Zhang and Z. Liu, *Chem. Soc. Rev.*, 2018, **47**, 5919-5945.
2   X. Cao, A. Halder, Y. Tang, C. Hou, H. Wang, J. Ø. Duus and Q. Chi, *Mater. Chem. Front.*, 2018, **2**, 1944-1986.
3   D. P. Dubal, N. R. Chodankar, D. H. Kim and P. Gomez-Romero, *Chem. Soc. Rev.*, 2018, **47**, 2065-2129.
4   L. Dai, D. W. Chang, J. B. Baek and W. Lu, *Small*, 2012, **8**, 1130-1166.
5   J. Zhang, Z. Xia and L. Dai, *Sci. Adv.*, 2015, **1**, e1500564.
6   X. Chen, R. Paul and L. Dai, *Natl. Sci. Rev.*, 2017, **4**, 453-489.

ARTICLE

Journal Name

7   J. Wang, S. Dong, B. Ding, Y. Wang, X. Hao, H. Dou. Y. Xia and X. Zhang, *Natl. Sci. Rev.*, 2017, **4**, 71-90.

8   M. F. El-Kady, Y. Shao and R. B. Kaner, *Nat. Rev. Mater.*, 2016, **1**, 16033.

9   B. Yao, J. Zhang, T. Kou, Y. Song, T. Liu and Y. Li, *Adv. Sci.*, 2017, **4**, 1700107.

10 Q. Ke and J. Wang, *J. Materiomics*, 2016, **2**, 37-54.

11 D. J. Bozym, S. Korkut, M. A. Pope and I. A. Aksay, *ACS Sustain. Chem. Eng.*, 2016, **4**, 7167-7174.

12 T. Li, N. Li, J. Liu, K. Cai, M. F. Foda, X. Lei and H. Han, *Nanoscale*, 2015, **7**, 659-669.

13 Z. F. Li, H. Zhang, Q. Liu, L. Sun, L. Stanciu and J. Xie, *ACS Appl. Mater. Interfaces*, 2013, **5**, 2685-2691.

14 M. Devi and A. Kumar, *Synth. Met.*, 2016, **222**, 318-329.

15 X. Li, Z. Wang, Y. Qiu, Q. Pan and P. Hu, *J. Alloys Compd.*, 2015, **620**, 31-37.

16 I. Shakir, *Electrochim. Acta*, 2014, **129**, 396-400.

17 S. Wang and R. A. W. Dryfe, *J. Mater. Chem. A*, 2013, **1**, 5279-5283.

18 X. Zhang, P. Yan, R. Zhang, J. Jin, J. Xu, C. Wu and H. Liu, *Int. J. Hydrogen Energy*, 2016, **41**, 6394-6402.

19 Y. Wang, J. Chen, J. Cao, Y. Liu, Y. Zhou, J. H. Ouyang and D. Jia, *J. Power Sources*, 2014, **271**, 269-277.

20 X. Wu, Y. Xu, Y. Hu, G. Wu, H. Cheng, Q. Yu, K, Zhang, W, Chen and C. Su, *Nat. Commun.*, 2018, **9**, 4573.

21 A. Shah, A. Zahid, H. Subhan, A. Munir, F. J. Iftikhar and M. Akbar, *Sustain. Energ. Fuels*, 2018, **2**, 1398-1429.

22 K. A. Worsley, I. Kalinina, E. Bekyarova and R. C. Haddon, *J. Am. Chem. Soc.*, 2009, **131**, 18153-18158.

23 M. Carmo, M. Linardi and J. G. R. Poco, *Appl. Catal. A Gen.*, 2009, **355**, 132-138.

24 D. Li, M. B. Müller, S. Gilje, R. B. Kaner and G. G. Wallace, *Nat. Nanotechnol.*, 2008, **3**, 101-105.

25 M. C. F. Soares, M. M. Viana, Z. L. Schaefer, V. S. Gangoli, Y. Cheng, V. Caliman, M. S. Wong and G. G. Silva, *Carbon*, 2014, **72**, 287-295.

26 X. Zhang, S. Chen, Q. Han and M. Ding, *J. Chromatogr. A*, 2013, **1307**, 135-143.

27 S. Verma and R. K. Dutta, *RSC Adv.*, 2015, **5**, 77192-77203.

28 J. A. Kenar, F. C. Felker and G. F. Fanta, *J. Appl. Polym. Sci.*, 2012, **126**, E418-E429.

29 D. J. Growney, O. O. Mykhaylyk, L. Middlemiss, L. A. Fielding, M. J. Derry, N. Aragrag, G. D. Lamb and S. P. Armes, *Langmuir*, 2015, **31**, 10358-10369.

30 A. M. Schwenke, S. Hoeppener and U. S. Schubert, *Adv. Mater.*, 2015, **27**, 4113-4141.

31 I. Bilecka and M. Niederberger, *Nanoscale*, 2010, **2**, 1358-1374.

32 T. J. Prior, J. A. Armstrong, D. M. Benoit and K. L. Marshall, *CrystEngComm*, 2013, **15**, 5838-5843.

33 Y. S. Jun, E. Z. Lee, X. Wang, W. H. Hong, G. D. Stucky and A. Thomas, *Adv. Funct. Mater.*, 2013, **23**, 3661-3667.

34 X. Cao, F. Shen, M. Zhang and C. Sun, *Sens. Actuators B Chem.*, 2014, **202**, 1175-1182.

35 G. F. Wang, H. Qin, X. Gao, Y. Cao, W. Wang, F. C. Wang, H. A. Wu, H. P. Cong and S. H. Yu, *Chem*, 2018, **4**, 896-910.

36 J. D. Wuest and A. Rochefort, *Chem. Commun.*, 2010, **46**, 2923-2925.

37 L. Zhang, B. Ji, K. Wang and J. Song, *Mater. Sci. Eng. B*, 2014, **185**, 129-133.

38 Z. H. Sheng, L. Shao, J. J. Chen, W. J. Bao, F. B. Wang and X. H. Xia, *ACS Nano*, 2011, **5**, 4350-4358.

39 H. Yan, Y. Chen and S. Xu, *Int. J. Hydrogen Energy*, 2012, **37**, 125-133.

40 M. S. Lee, H. J. Choi, J. B. Baek and D. W. Chang, *Appl. Energy*, 2017, **195**, 1071-1078.

41 L. Ma, R. Liu, H. Niu, L. Xing, L. Liu and Y. Huang, *ACS Appl. Mater. Interfaces*, 2016, **8**, 33608-33618.

42 Y. J. Oh, J. J. Yoo, Y. I. Kim, J. K. Yoon, H. N. Yoon, J. H. Kim and S. B. Park, *Electrochim. Acta*, 2014, **116**, 118-128.

43 H. L. Guo, S. Peng, J. H. Xu, Y. Q. Zhao and X. Kang, *Sens. Actuators B Chem.*, 2014, **193**, 623-629.

44 Y. Xu, Z. Lin, X. Huang, Y. Liu, Y. Huang and X. Duan, *ACS Nano*, 2013, **7**, 4042-4049.

45 X. Zhang, R. Zhang, Z. Zhen, W. Lai, C. Yang, F. Kang and H. Zhu, *Nano Energy*, 2017, **40**, 224-232.

46 J. Yun, D. Kim, G. Lee and J. S. Ha, *Carbon*, 2014, **79**, 156-164.

47 D. K. Kim, N. D. Kim, S. K. Park, K. D. Seong, M. Hwang, N. H. You and Y. Z. Piao, *J. Power Sources*, 2018, **380**, 55-63.

48 H. Xu, X. Hu, X. Yang, Y. Sun, C. Hu and Y. Huang, *Adv. Energy Mater.*, 2015, **5**, 1401882.

49 L. Xu, M. Jia, Y. Li, S. Zhang and X. Jin, *RSC Adv.*, 2017, **7**, 31342-31351.

50 J. Cao, Y. Wang, J. Chen, X. Li, F. C. Walsh, J. H. Ouyang, D. Jia and Y. Zhou, *J. Mater. Chem. A*, 2015, **3**, 14445-14457.

51 X. Lang, A. Hirata, T. Fujita and M. Chen, *Nat. Nanotechnol.*, 2011, **6**, 232-236.

52 Z. S. Wu, A. Winter, L. Chen, Y. Sun, A. Turchanin, X. Feng and K. Müllen, *Adv. Mater.*, 2012, **24**, 5130-5135.

53 S. Wang, B. Pei, X. Zhao and R. A. W. Dryfe, *Nano Energy*, 2013, **2**, 530-536.

54 C. Choi, S. H. Kim, H. J. Sim, J. A. Lee, A. Y. Choi, Y. T. Kim, X. Lepró, G. M. Spinks, R. H. Baughman and S. J. Kim, *Sci. Rep.*, 2015, **5**, 9387.

55 L. Kou, T. Huang, B. Zheng, Y. Han, X. Zhao, K. Gopalsamy, H. Sun and C. Gao, *Nat. Commun.*, 2014, **5**, 3754.

56 P. Huang, C. Lethien, S. Pinaud, K. Brousse, R. Laloo, V. Turq, M. Respaud, A. Demortière, B. Daffos, P. L. Taberna, B. Chaudret, Y. Gogotsi and P. Simon, *Science*, 2016, **351**, 691-695.

57 Z. Wang, J. Cheng, J. Zhou, J. Zhang, H. Huang, J. Yang, Y. Li and B. Wang, *Nano Energy*, 2018, **50**, 106-117.

58 J. Pu, X. Wang, T. Zhang, S. Li, J. Liu and K. Komvopoulos, *Nanotechnology*, 2016, **27**, 045701.

59 U. N. Maiti, J. Lim, K. E. Lee, W. J. Lee and S. O. Kim, *Adv. Mater.*, 2014, **26**, 615-619.

60 A. Sumboja, C. Y. Foo, X. Wang and P. S. Lee, *Adv. Mater.*, 2013, **25**, 2809-2815.

61 C. Y. Foo, A. Sumboja, D. J. H. Tan, J. Wang and P. S. Lee, *Adv. Energy Mater.*, 2014, **4**, 1400236.

62 Z. Xiong, C. Liao, W. Han and X. Wang, *Adv. Mater.*, 2015, **27**, 4469-4475.

63 Z. Weng, Y. Su, D. W. Wang, F. Li, J. Du and H. M. Cheng, *Adv. Energy Mater.*, 2011, **1**, 917-922.

64 Z. Lv, Y. Tang, Z. Zhu, J. Wei, W. Li, H. Xia, Y. Jiang, Z. Liu, Y. Luo, X. Ge, Y. Zhang, R. Wang, W. Zhang, X. J. Loh and X. Chen, *Adv. Mater.*, 2018, **30**, 1805468.

65 X. Wu, G. Wu, P. Tan, H. Cheng, R. Hong, F. Wang and S. Chen, *J. Mater. Chem. A*, 2018, **6**, 8940-8946.

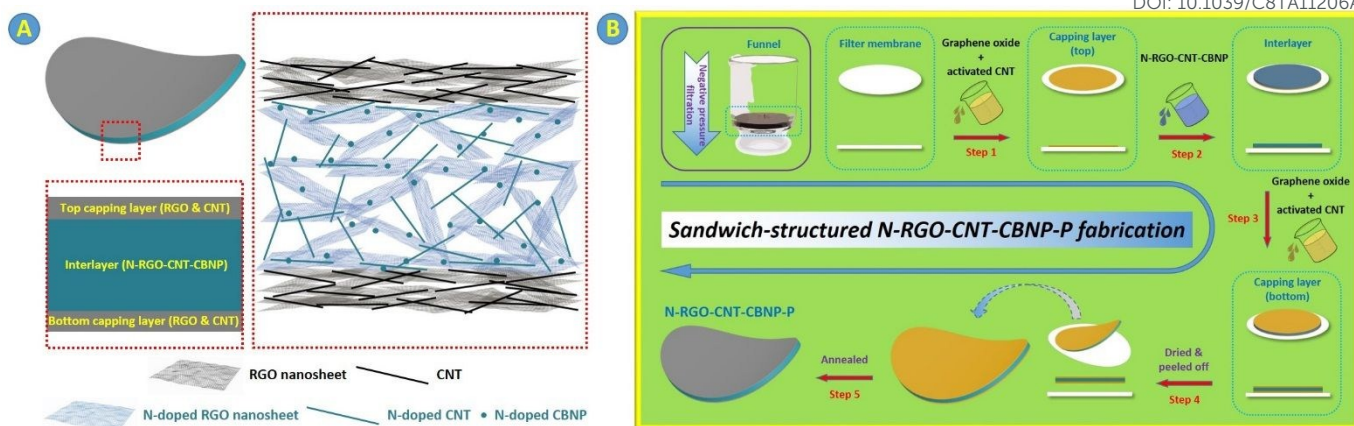66 S. S. Lee, K. H. Choi, S. H. Kim and S. Y. Lee, *Adv. Funct. Mater.*, 2018, **28**, 1705571

Fig. 1. Schematic illustration of (A) the N-RGO-CNT-CBNP-P structure and (B) the processes for fabricating N-RGO-CNT-CBNP-Ps. Not drawn to scale.
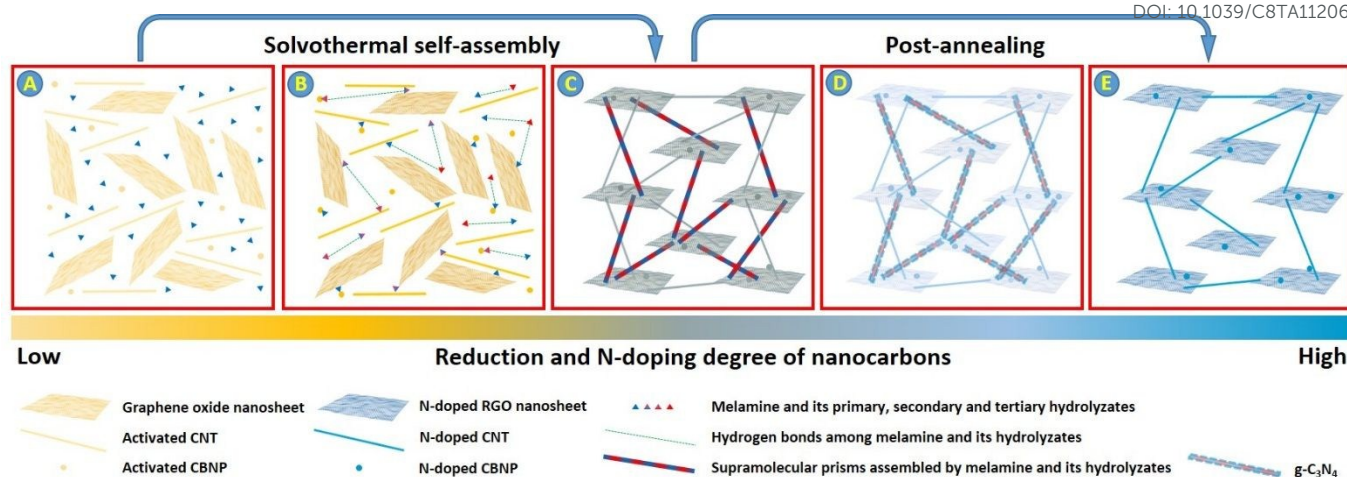
Fig. 2. Schematic illustration of the N-RGO-CNT-CBNP synthesis. (A) The starting mixture containing oxidized nanocarbons and melamine. (B, C) Two stages of the microwave-assisted solvothermal self-assembly process. (D, E) Two stages of the post-annealing process. Not drawn to scale.
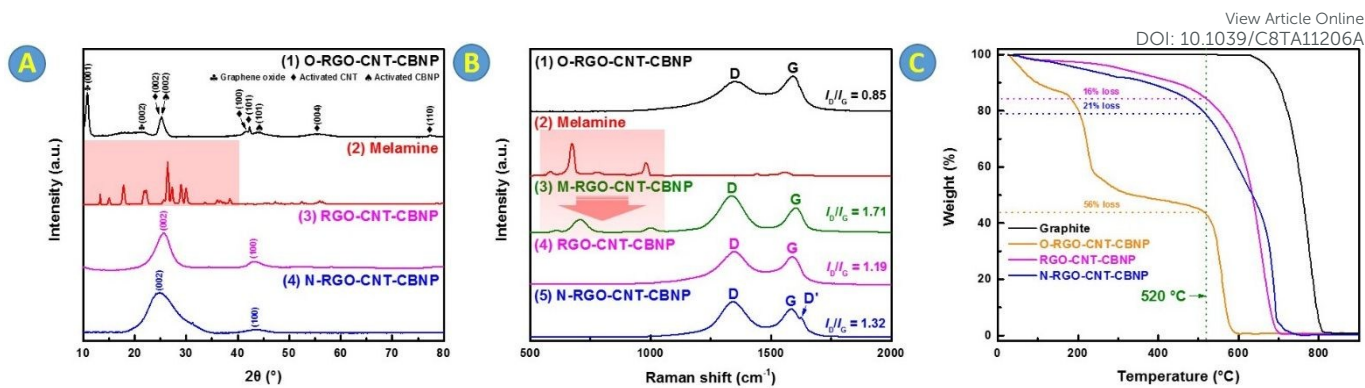
Fig. 3. (A) XRD patterns of O-RGO-CNT-CBNP, melamine, RGO-CNT-CBNP and N-RGO-CNT-CBNP. (B) Raman spectra of O-RGO-CNT-CBNP, melamine, M-RGO-CNT-CBNP, RGO-CNT-CBNP and N-RGO-CNT-CBNP. (C) TGA curves of graphite, O-RGO-CNT-CBNP, RGO-CNT-CBNP and N-RGO-CNT-CBNP.
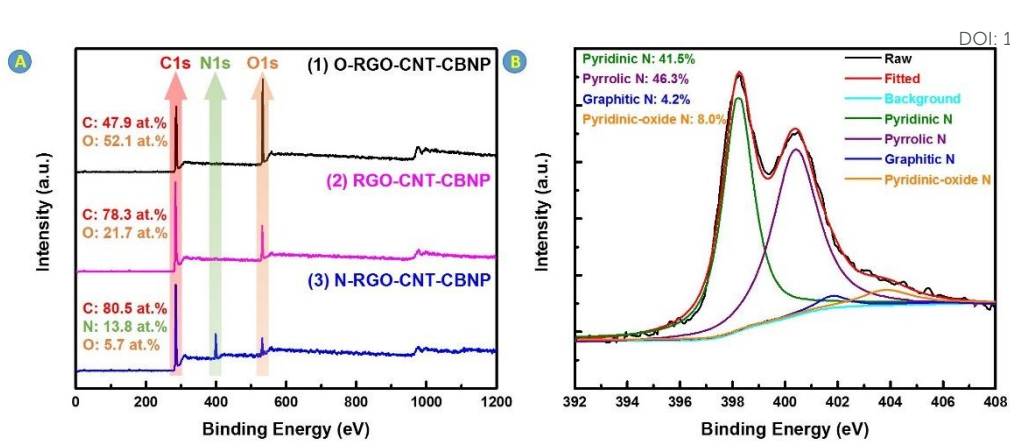
Fig. 4. (A) XPS survey spectra of O-RGO-CNT-CBNP, RGO-CNT-CBNP and N-RGO-CNT-CBNP. (B) A high-resolution XPS N1s spectrum of N-RGO-CNT-CBNP.
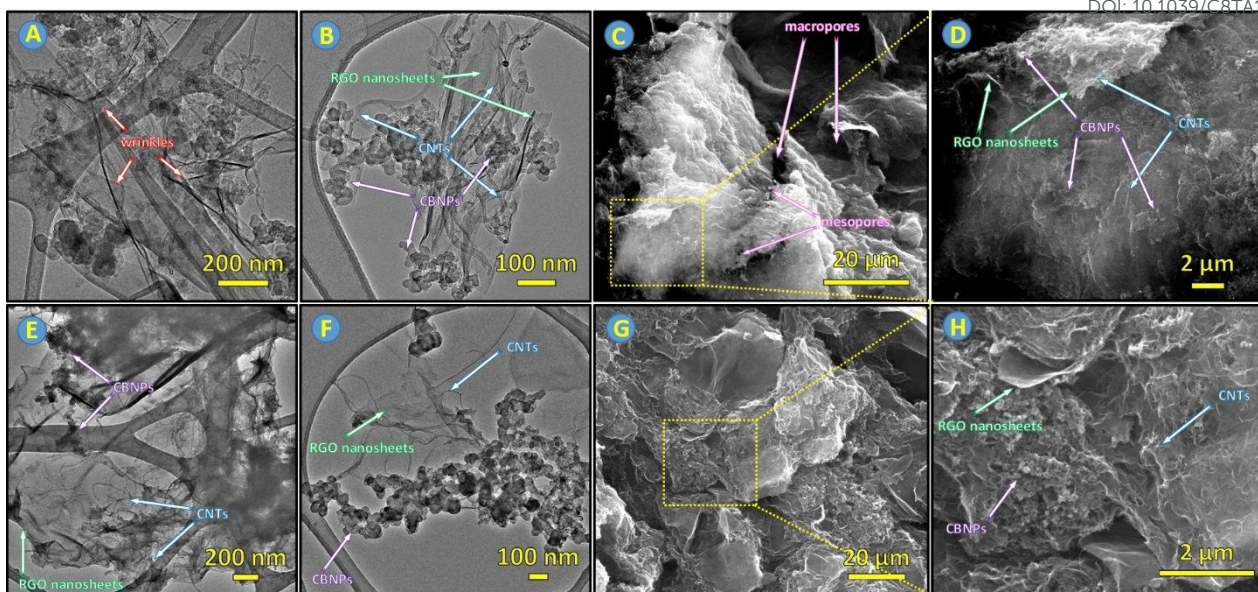
Fig. 5. (A, B) TEM images of N-RGO-CNT-CBNP. (C, D) SEM images of N-RGO-CNT-CBNP. (E, F) TEM images of RGO-CNT-CBNP. (G, H) SEM images of RGO-CNT-CBNP.
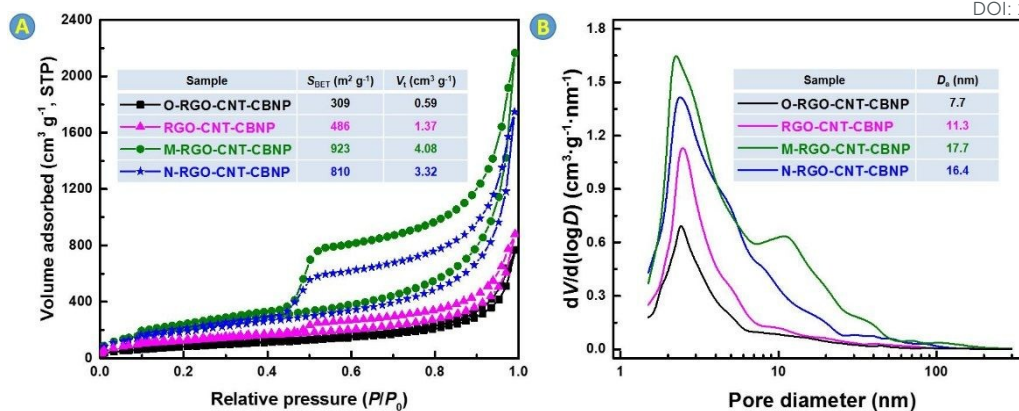
Fig. 6. (A) Nitrogen adsorption-desorption isotherms of O-RGO-CNT-CBNP, RGO-CNT-CBNP, M-RGO-CNT-CBNP and N-RGO-CNT-CBNP. The inset table shows the calculated s_{BET} and V_t. STP: the standard condition for temperature and pressure. (B) Pore size distributions of O-RGO-CNT-CBNP, RGO-CNT-CBNP, M-RGO-CNT-CBNP and N-RGO-CNT-CBNP. The inserted table shows the measured average diameter of pores (D_a).
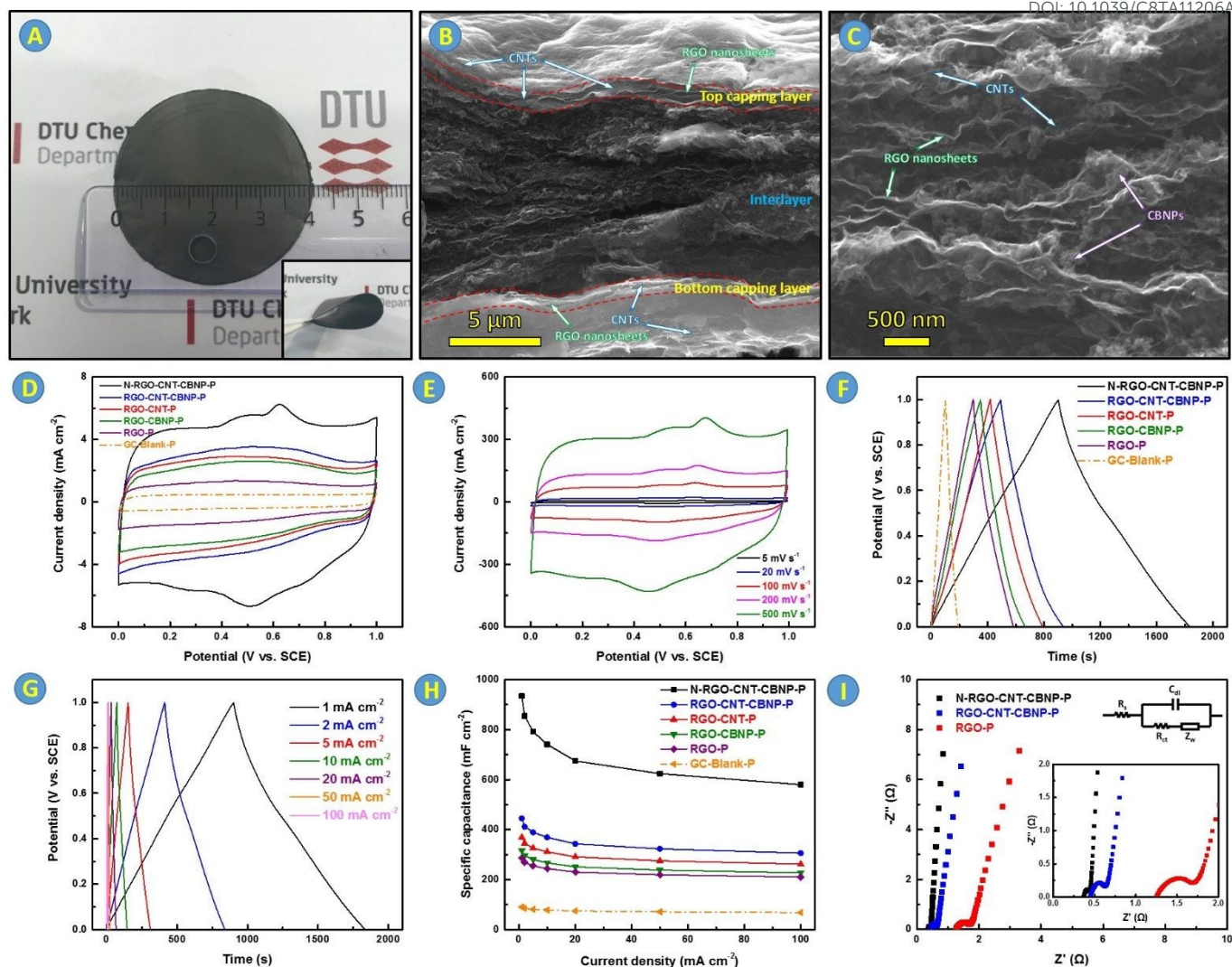
Fig. 7. (A) A digital photograph of a piece of as-prepared N-RGO-CNT-CBNP-P. Inset: a curved N-RGO-CNT-CBNP-P demonstrating its flexibility. (B) A cross-sectional SEM image of an N-RGO-CNT-CBNP-P. (C) A cross-sectional SEM image of the interlayer of an N-RGO-CNT-CBNP-P. (D) CV curves of different paper electrodes at a scan rate of 5 mV s^{-1}. (E) CV curves the N-RGO-CNT-CBNP-P at different scan rates ranging from 5 to 500 mV s^{-1}. (F) GCD curves of different paper electrodes at a current density of 1 mA cm^{-2}. (G) GCD curves of the N-RGO-CNT-CBNP-P at different current densities ranging from 1 to 100 mA cm^{-2}. (H) Comparison of areal specific capacitances of different paper electrodes at different current densities. (I) Nyquist plots of an N-RGO-CNT-CBNP-P, a RGO-CNT-CBNP-P and a RGO-P. Insets: (lower) A magnified portion of the high frequency region and (upper) the equivalent circuit model to fit the Nyquist plots.
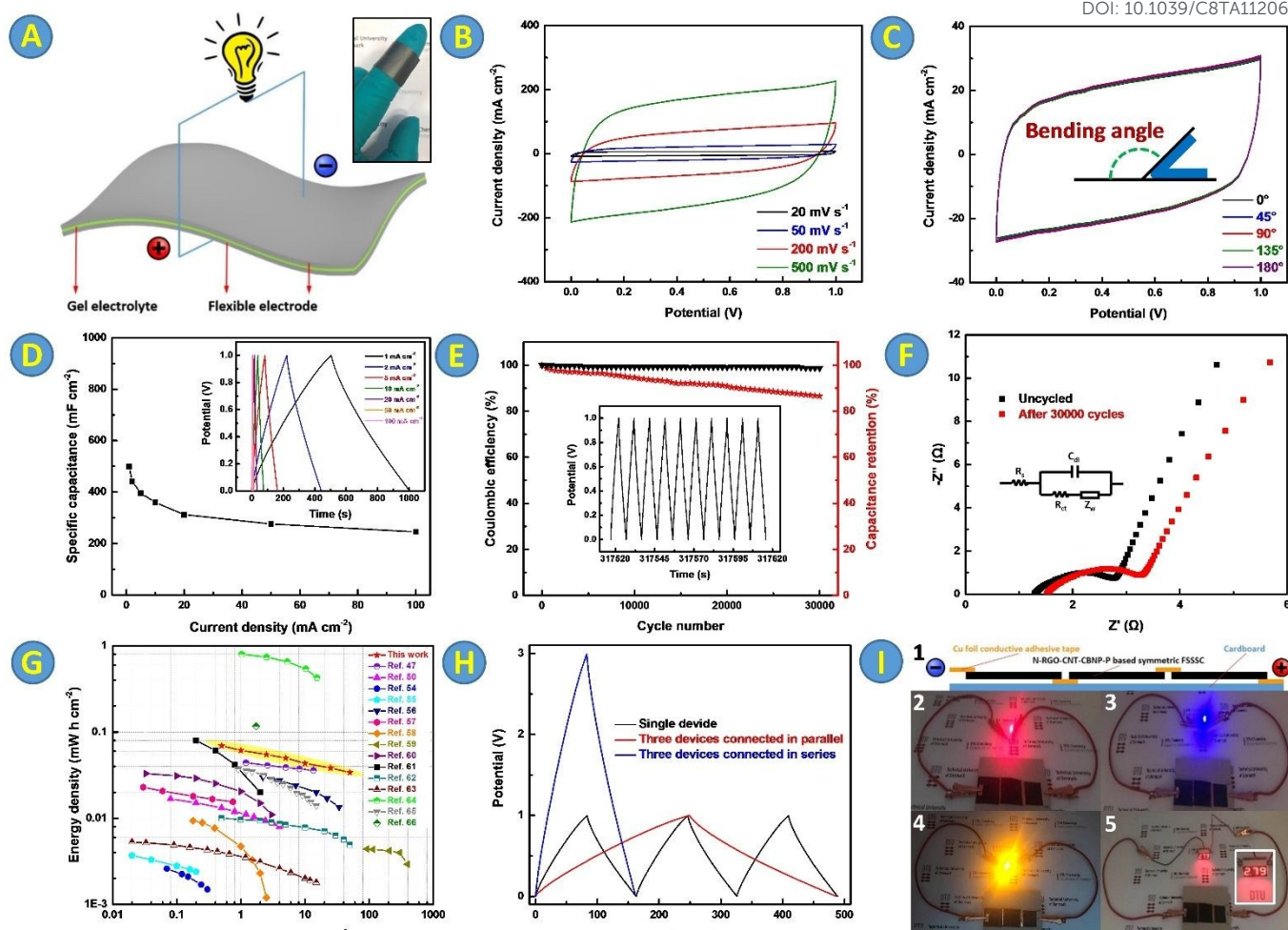
Fig. 8. (A) Schematic showing the structure of an N-RGO-CNT-CBNP-P based symmetric FSSSC. Inset: the FSSSC mounted on a finger showing its flexibility. (B) CV curves of the FSSSC measured at different scan rates ranging from 20 to 500 mV s^{-1}. (C) CV curves of the FSSSC at different bending angles at a scan rate of 50 mV s^{-1}. (D) Comparison of areal specific capacitances of the FSSSC at different current densities. Inset: GCD curves of the FSSSC at different current densities ranging from 1 to 100 mA cm^{-2}. (E) Cyclic stability of the FSSSC at a current density of 50 mA cm^{-2}. Inset: the GCD curves of the last ten cycles. (F) EIS curves of the FSSSC before and after 30,000 charge-discharge cycles at a current density of 50 mA cm^{-2}. Inset: the equivalent circuit. (G) Areal Ragone plots of the FSSSC and some other reported supercapacitor devices. (H) GCD curves of power devices based on a single FSSSC, three parallel-connected FSSSCs and three series-connected FSSSC at a current density of 5 mA cm^{-2}. (I) 1: Schematic showing a structural side view of the power device based on three series-connected FSSSCs for the actual power supply tests. 2, 3 and 4: Photos showing the power device was capable of powering a red, blue or yellow LED. 5: A photo showing the power device used for powering a small digital voltmeter. Inset of 5: An enlarged photo showing the measured open circuit voltage of the FSSSC.

For TOC entry
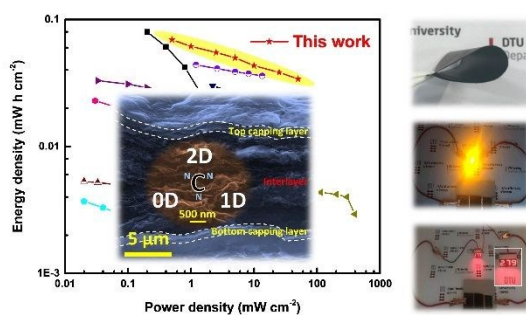
Nitrogen-doped hybrid-dimensional nanocarbons are architected into special structures and used for fabrication of solid-state flexible supercapacitors showing high-performance energy storage capacity.